Solar Energy 230 (2021) 591–597

Contents lists available at ScienceDirect

Solar Energy

journal homepage: www.elsevier.com/locate/solener

Interfacial engineering with NiO_x nanofibers as hole transport layer for carbon-based perovskite solar cells

S.N. Vijayaraghavan [a], Jacob Wall [a], Harigovind G. Menon [a], Xiaomeng Duan [a], Liping Guo [a], Al Amin [a], Xiao Han [a], Lingyan Kong [b], Yufeng Zheng [c], Lin Li [a], Feng Yan [a,*]

[a] Department of Metallurgical and Materials Engineering, The University of Alabama, Tuscaloosa, AL 35487, USA
[b] Department of Human Nutrition and Hospitality Management, The University of Alabama, Tuscaloosa, AL 35487, USA
[c] Department of Chemical and Materials Engineering, University of Nevada Reno, 1664 N. Virginia St., Reno, NV 89557, USA

ARTICLE INFO

Keywords:
Nickel oxide
Nanofibers
Hole-transport layer
Spin-coating
Low-cost
High-stability
Perovskite solar cells

ABSTRACT

Although perovskite solar cells (PSCs) have made revolutionary progress in terms of power conversion efficiency (PCE), to achieve long-term stability and low-cost device manufacturing for commercialization of the devices, selection of proper hole transport layer (HTL) and affordable back contact are still crucial to realize the upscale manufacturing. However, the carbon-based perovskite still faces great challenges to further improve the device performance due to the low quality of the carbon/perovskite interface. Inorganic NiO_x is a superior HTL candidate due to its favorable energy band alignment, superior chemical stability, high hole mobility, and low-cost manufacturing. To address the poor interface quality of the carbon-based PSCs, we report electrospun NiO_x fibers as an effective HTL, resulting in highly efficient device performance of PCEs up to 13.73% when deployed in our carbon-based PSCs. NiO_x has been introduced as an interfacial layer between the perovskite and the carbon counter electrode to study its impact on interfacial modification and device performance.

1. Introduction

Perovskite solar cells (PSCs) represent the most promising next-generation solar technology due to the high absorption coefficient, high mobility, and long diffusion length, with rapidly improved power conversion efficiency (PCE) up to 25.5% in the past decade and close to 80% of the theoretical efficiency (Yoo et al., 2021). However, it is critical to further reduce the cost of the PSCs to upscale manufacture the corresponding solar module. Particularly, the high-efficiency PSCs were produced in the laboratory with noble back contact, such as gold and silver, which is not feasible for large volumetric manufacturing. Carbon electrode was considered as a low-cost back contact with suitable work function for the perovskite (Hadadian et al., 2020). Particularly, high efficiency carbon-based PSCs still need to work with organic HTLs, such as spiro-OMeTAD and P3HT (Chu et al., 2019; Hawash et al., 2018; Jung and Park, 2015). To get the best out of spiro-OMeTAD, it requires dopants such as lithium bis(trifluoromethanesulfonyl)-imide (LiTFSI), *tert*-butylpyridine (t-BP), and a Co (III) complex to improve the hole conductivity, while adding these dopants will compromise the stability of the device (Wang et al., 2018).

So, it was necessary to find a suitable replacement for organic HTL that didn't have these issues. P-type metal oxide semiconductors possess several attractive properties such as transparency in the visible region, good thermal and chemical stabilities, excellent hole transport properties, and easy tuning of the valence band maximum. For instance, NiO_x-based HTL stands out because of its large bandgap, and deep-valence band position that helps in the extraction of holes (Jeng et al., 2014; Kaneko et al., 2019; Manders et al., 2013; Saranin et al., 2021). Despite boasting several benefits, NiO_x is mostly used with p-i-n structured PSCs because the precursor solution for NiO_x uses a polar solvent that can damage the perovskite layer (Singh et al., 2021). Though recently Icli et. al. demonstrated using IPA as the solvent for NiO_x to fabricate the regular n-i-p structure PSC, the resulting device could only deliver a PCE of 10.9% due to the rough surface (Icli and Ozenbas, 2018). Kaneko et. al. then further modified the NiO_x nanoparticles (NPs) by using hexanoic acid as a surfactant to prevent the agglomeration of the NPs and to obtain a smooth layer of NiO_x. The resulting device delivered an impressive PCE of 13.1% (Kaneko et al., 2019). Despite these attempts, works on incorporating NiO_x HTL in the n-i-p structured devices are few.

Promisingly, one-dimensional (1D) nanostructured materials such as

* Corresponding author.
E-mail address: fyan4@ua.edu (F. Yan).

https://doi.org/10.1016/j.solener.2021.10.039
Received 7 July 2021; Received in revised form 21 September 2021; Accepted 11 October 2021
Available online 28 October 2021

nanorods, nanowires, and nanofibers (NFs) have gained considerable traction recently due to their increasing demands in technological applications. They are being increasingly used for diverse applications in photonics and nano-electronics (Wang and Santiago-Avilés, 2003). Especially, carbon NFs have been gaining considerable attention for its use in the PSCs due to the improved device performance and stability (Habisreutinger and Blackburn, 2021; Schulz et al., 2016). However, limited work has been done on NiOx NFs for the PSCs application. Due to the strong dependence of its properties on morphology, NiO_x NFs are of great practical importance in several engineering applications such as capacitors, photocatalysis, sensing, and other chemical catalysis (Liu et al.; Macdonald et al., 2014; Nakasa et al., 2005; Zang et al., 2014). Of all the physical techniques that have been successfully employed for their synthesis, electrospinning has turned out to be a promising choice because of its simplicity, scaling capability, economy, ability to synthesize long continuous fibers, and control over the NF morphology (Khalil et al., 2014; Sigmund et al., 2006). Such synthesized NFs have shown promising potential in several engineering domains including solar energy conversion owing to their adventitious properties such as large surface-to-volume ratio, high efficiency, fast charge transportation, high sensitivity, appreciable physical and chemical properties (Kim et al., 2011; Liu et al., 2011; Shim et al., 2009; Xia et al., 2003).

In this work, we have successfully synthesized NiO_x NFs as HTL for PSC by electrospinning technique and studied the optoelectronic properties of the fibers. We systematically investigated the NiOx NFs HTL for the carbon-based PSCs. We have found a significant improvement of the PCE from 10.11% for HTL-free devices to 13.73% for NiOx NF-based devices. On the other hand, devices with NiO_x NPs as HTL (12.94%) delivered a lower PCE when compared with the one using NFs, suggesting that the NiO_x NFs could facilitate a rapid charge extraction.

2. Experimental section

2.1. Materials

Cellulose acetate (Acros Organics, acetyl content ~ 39.8%), nickel (II) nitrate hexahydrate (Alfa Aesar, 99.9985%), nickel oxide nanoparticles (US Research Nanomaterials, 99%, 10–20 nm), PbI_2 (Sigma-Aldrich, 99.999%), $PbBr_2$ (Alfa Aesar, 99.98%), formamidinium iodide (FAI, GreatCellSolar), methylammonium bromide (MABr, GreatCellSolar), CsI (BeanTown Chemical, 99.9%), $SnCl_2{\cdot}2H_2O$ (Acros Organics, 97%), and thiourea (Alfa Aesar, 99%) were used without further purification. Dimethyl sulfoxide (DMSO) and dimethyl formamide (DMF) were purchased from Sigma-Aldrich and used as received.

2.2. NiOx NPs and NFs synthesis

NiOx NPs were synthesized following the previously reported work (Guo et al., 2021). Briefly, 0.05 mol Nickel (II) nitrate hexahydrate, i.e., $Ni(NO_3)_2{\cdot}6H_2O$ was dissolved in 10 mL deionized water (DIW). Then NaOH solution was added into the as-dissolved $Ni(NO_3)_2$ solution under vigorous stirring until the solution turned into a turbid green color with a pH of 10. The solution was then filtered to obtain the precipitation which was washed by DIW to get rid of the impurities. The wet precipitate was dried at 80 °C for 8 h and then ground into powder, which was then annealed in air at 270 °C for 2 h to get the NiOx NPs. NiOx NFs were synthesized as below: Nickel (II) nitrate hexahydrate was added to the cellulose acetate (CA) 12% (w/v) solution with acetone as solvent. After completely dissolved solution (0.5 mg/10 mL) formation, the spinning precursor solution was then loaded into a 10-mL syringe (Becton, Dickinson and Company, Franklin Lakes, NJ, USA) with a 22-gauge blunt needle (Hamilton Company, Reno, NV, USA) as the spinneret. The nickel nitrate-loaded fibers were then spun as explained in our previous work (Angel et al., 2020). After the spinning process, the fibers formed on the aluminum foil directly beneath the spinneret tip were collected and annealed at 400 °C for 30 min in a box oven with an adequate supply of oxygen flow.

2.3. Solar cells fabrication

PSCs were fabricated as mentioned in our previous work (Vijayaraghavan et al., 2020). In brief, In doped SnO_2 (ITO) substrates were successively sonicated in detergent solution, DIW, acetone, and IPA, followed by a 30 min UV-Ozone treatment. The SnO_2 precursor was then spin-coated on the ITO substrates at 3500 rpm for 30 s and then annealed at 180 °C for 1 h. The SnO_2 coated ITO substrates were transferred to the dry nitrogen-filled glovebox after a 10-minute UV-Ozone treatment. The triple cation perovskite precursor was then deposited by a two-step spin-coating procedure: 1000 rpm 10 s followed by 6000 rpm 30 s. Diethyl ether (DEE) was dropped on the spinning substrate 25 s before the end of spin-coating. The NiO_x HTL was coated using the NP/NF solution in chlorobenzene (20 mg/mL) at 4000 r.p.m. for 30 s. Finally, 25 μm carbon paste was doctor bladed onto the cells.

2.4. Materials and device characterization

The morphology of the electrospun fibers and the surface morphology of the perovskite films with NiO_x NFs and NPs were studied using a Thermo Scientific Apreo scanning electron microscope (SEM). Thermal properties of the obtained fibers were characterized at a rate of 20 °C/min heating from 25 °C to 550 °C under N_2 atmosphere using a TA differential scanning calorimetry (DSC 250). The distribution of chemical elements in the fibers and the films were studied using the energy-dispersive X-ray spectroscopy (EDS) equipped with the SEM. Park XE-70 atomic force microscope (AFM) was used to study the surface roughness of the perovskite films with and without the NiO_x HTLs. The wide-angle X-ray diffraction (XRD) patterns of the annealed fibers were studied using a Philips XPert Materials Research Diffractometer with a 45 kV, 40 mA Cu Kα radiation (λ = 0.15405 nm). The X-ray photoelectron spectroscopy (XPS) was recorded using the Kratos Axis XPS system equipped with a monochromated Al X-ray source. The electrical characterization of the fabricated PSCs with an active area of 0.08 cm^2 were recorded using a solar simulator (Newport, Oriel Class AAA 94063A, 1000-Watt Xenon light source) with a Keithley 2420 source meter under simulated AM 1.5G (100 mW/cm^2) solar irradiation. The light intensity was calibrated using a silicon reference cell (Newport, 91150 V, certified by National Renewable Energy Lab). The electrochemical impedance spectroscopy (EIS) measurement were measured using an electrochemical workstation (Gamry Instruments). The EIS measurements were measured by applying a bias of the open-circuit voltage with frequencies ranging from 10^6 Hz to 1 Hz.

3. Results and discussion

Fig. 1(a) shows the schematic representation of the electrospinning process of the NiO_x NFs. The as-span $Ni(NO_3)_2$ fibers and post-annealed fibers at 400 °C for 30 min are shown, respectively. The white CA fibers with $Ni(NO_3)_2$ were obtained at room temperature. Then, the $Ni(NO_3)_2$ fibers were annealed at 400 °C in air to obtain the NiOx NFs. The thermal properties of the $Ni(NO_3)_2$-CA fibers were determined using the DSC, where the exothermic peaks shift to a higher temperature with addition of the $Ni(NO_3)_2$. The decomposition of the $Ni(NO_3)_2$ around 250 °C was observed, which is in line with the pure $Ni(NO_3)_2$ decomposition (Brockner et al., 2007). Fig. 1(c) shows that the scanning electron microscopy (SEM) images of the synthesized NiO_x fibers after annealing at 400 °C for 30 min. It is observed that the NiOx NFs prepared by electrospinning becomes porous with one-dimensional (1D) fiber morphology after thermal treatment. The annealed fibers have a diameter of ~100 nm in average, while they are uniform along the entire length. Previous study by Cheng et. al. suggest that the formation of NFs were influenced by the solvent evaporation rate and polymer burning rate during the sintering process (Zhang et al., 2010).

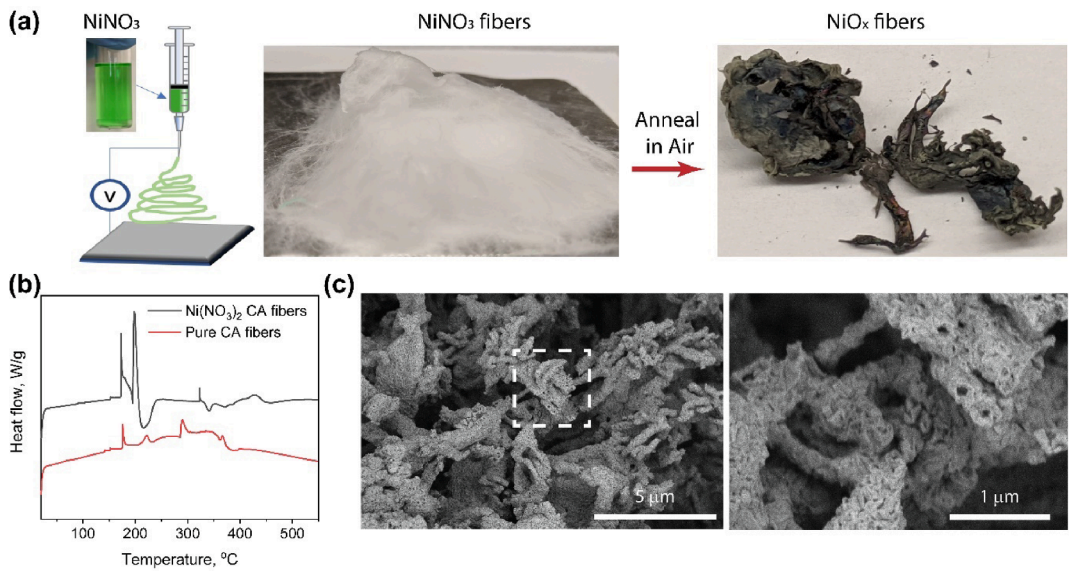

Fig. 1. (a) Schematic representation of electrospinning NiO_x NFs, and photographic images of as-spun and sintered fibers. The $NiNO_3$ dissolved into the CA/acetone solution was shown. (b) Differential scanning calorimetry (DSC) of cellulose acetate (CA) and $Ni(NO_3)_2$ -CA fibers, and (c) SEM images of annealed NiO_x fibers at 400 °C for 30 min under different magnification.

Fig. 2(a) shows the XRD spectra of the pure CA, NiOx NPs, and NFs, respectively. The diffraction peaks are indexed as (100), (200), and (220). suggesting a face-centered cubic unit cell of NiOx (Harilal et al., 2017). The particle size was calculated according to the Scherrer formula, i.e., $D_{hkl} = \frac{K\lambda}{\beta_{hkl}cos\theta}$, where K is the particle shape factor, λ is X-ray wavelength, β_{hkl} is the half-width of *(hkl)* reflection, and θ bragg angle

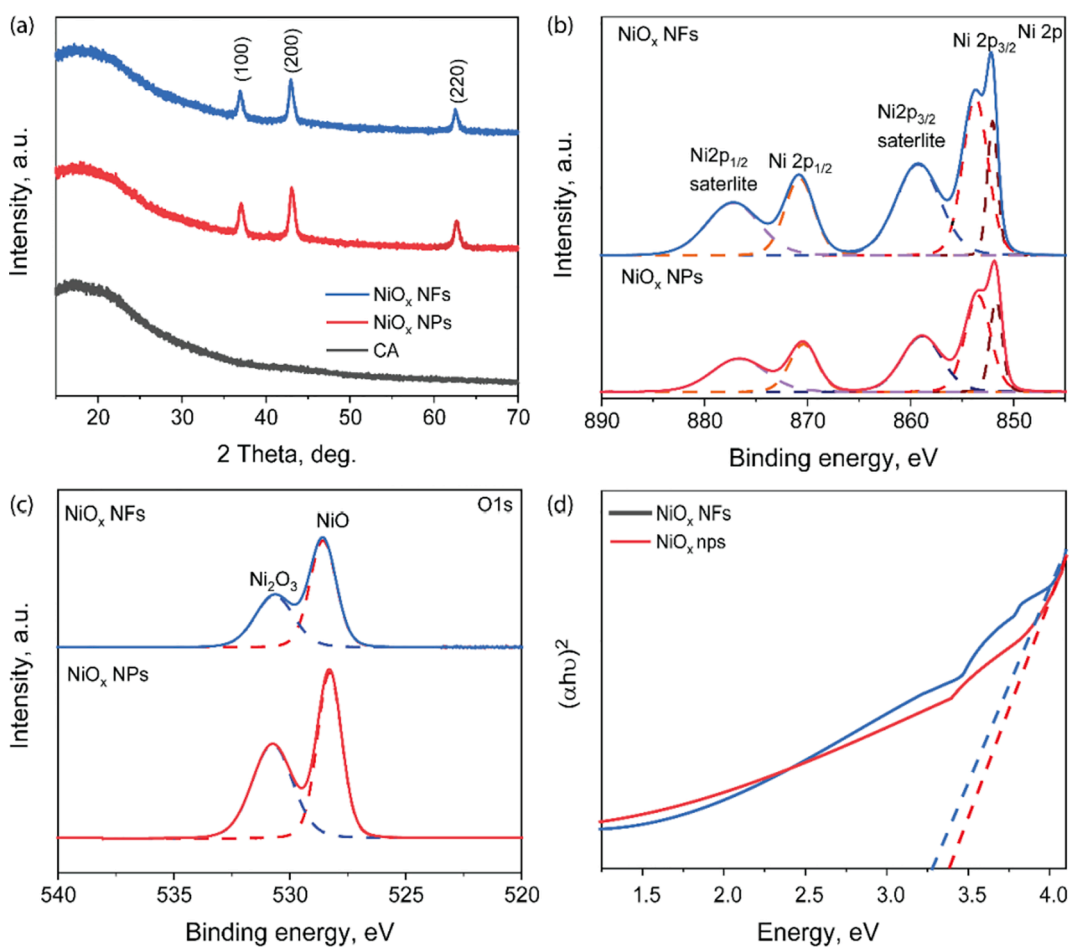

Fig. 2. (a) XRD pattern of as-prepared pure CA fibers, NiO_x NPs, and NiO_x NFs. XPS spectra of (b) Ni 2p and (c) O 1s core level of NiO_x NFs, and NPs. (d) Tauc plot was used to estimate the bandgap of NiO_x NFs and NPs.

corresponding to *(hkl)* reflection (Bokuniaeva and Vorokh, 2019). The particles size for the NiOx NPs was calculated to be ~40 nm with a K ~ 0.9 as a spherical crystal, while the particles size for the NiOx NFs was calculated to be ~90 nm with a K ~ 2 as a tetrahedron crystal for the fibers (Langford and Wilson, 1978).

Supporting information Fig. S1 presents the XRD spectra of perovskite film. The XRD patterns indicate that the perovskite structure. A (001) diffraction peak corresponding to PbI_2 plane at 12.4° was observed in the XRD spectrum, which is associated with the slightly PbI_2 rich in the precursor (Wang et al., 2017). The bandgap of 1.61 eV of the perovskite film was determined using the UV–Vis transmittance spectrum of perovskite film, as shown in supporting information Fig. S2.

The samples were then analyzed for XPS to examine the factual valence states and constitutions within the samples. Fig. 2 (b) shows the high-resolution spectra of Ni 2p, and Fig. 2 (c) shows the high-resolution spectra of O 1s of NiO_x NFs and NPs respectively. The Ni 2p region for NFs comprises four easily discernible features: Ni $2p_{3/2}$ main peak and its satellite at ~852 eV and ~860 eV, and the Ni $2p_{1/2}$ main peak and its satellite at ~871 eV and ~877 eV respectively. This is a clear indication that Ni exists in +2 oxidation states. The secondary $2p_{3/2}$ peak observed at ~855 eV is designated to Ni^{3+} oxidation state in NiOOH and Ni_2O_3 due to the Ni^{2+} vacancies because of excess oxygen or deficiency in nickel. The presence of NiOOH can be attributed to the surface adsorption of water and the formation of hydroxides. This is clear evidence that the NiO_x is non-stoichiometric with significant Ni^{2+} vacancies, which makes it a p-type material, and hence a suitable candidate as an HTL, while pure stoichiometric NiO acts as an insulator (Icli and Ozenbas, 2018). No apparent shift was observed for the Ni 2p peaks for NiO_x NP indicating that the major components of the NiO_x remain unchanged. The spectra of O 1s has a peak at ~528 eV that corresponds to the lattice oxygen in NiO_x, and the other peak corresponds to the hydroxylation that has occurred when films have been briefly exposed to the ambient environment (Hayat et al., 2019; Peck and Langell, 2012). The optical band gap was estimated using Tauc plot: $(\alpha h\nu)^{1/r}$ vs energy of the photons, where r represents the nature of the transition of the charge carriers and r = ½ for direct bandgap materials. The bandgap was found by extrapolating the linear region of the curve to $(\alpha h\nu)^2 = 0$. The bandgap was observed to be ~3.28 and ~3.38 eV for the NFs and NPs, respectively, which is similar to values reported previously (Hosny, 2011).

The surface morphologies of the bare perovskite, NiO_x NFs, and NPs deposited on the perovskite layer were studied by SEM as shown in Fig. 3 (a)-(c). The nanoscale NiOx NPs and NiOx NFs were dissolved in a non-polar solvent, e.g., chlorobenzene, which can be directly spin-coated on the perovskite films as an HTL without decomposing the perovskite film. The NiOx NPs and NFs are uniformly distributed on the perovskite and confirmed by the EDS mapping corresponding to the Ni element. To evaluate the surface roughness variation without and with the NiOx HTLs, AFM surface morphologies were collected as shown in Fig. 3 (g)-(i). The as-deposited perovskite film possessed a surface root-mean-square (RMS) roughness ~6.35 nm. It is shown that the NiOx NPs made the perovskite layer smoother up to RMS ~ 5.41 nm, while the NiOx NFs could further increase the surface roughness to RMS ~ 7.90 nm. This can be because the NiOx NFs might be embedded in the film and sticking out of the plane. For carbon-based PSCs, this can be advantageous as the carbon electrode is mesoporous, and hence these fibers, that are out of the plane of the perovskite film, can be embedded into the carbon electrode, thereby increasing the effective contact area between the fibers and the carbon, and hence, efficient extraction of holes comes from the perovskite (Fig. 3(a)).

Fig. 4(a) shows a schematic of the perovskite/Carbon interface with and without NiO_x NFs and NP as HTL. Photoexcitation occurs in the

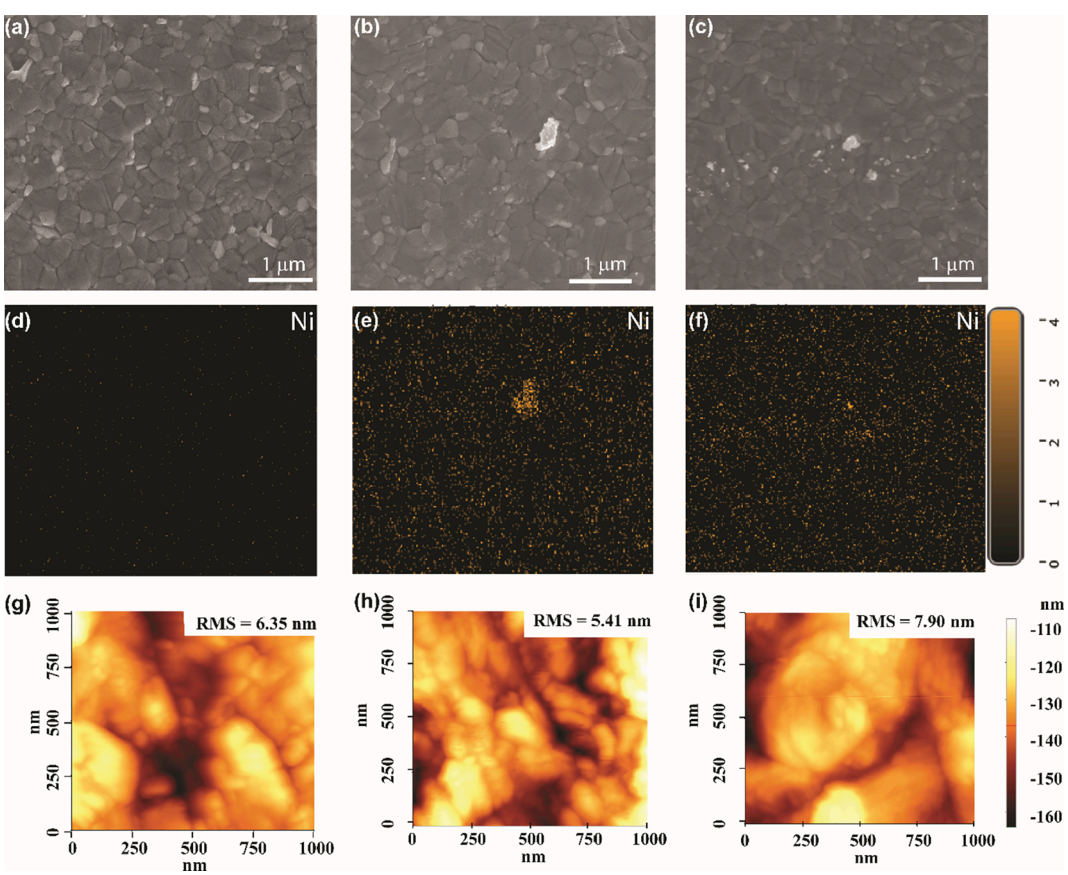

Fig. 3. (a-c) Surface morphology, (d-f) EDS mapping of Ni and (g-i) large scale non-contact AFM image showing the topography of bare perovskite, perovskite with NiO_x NPs, and NFs respectively.

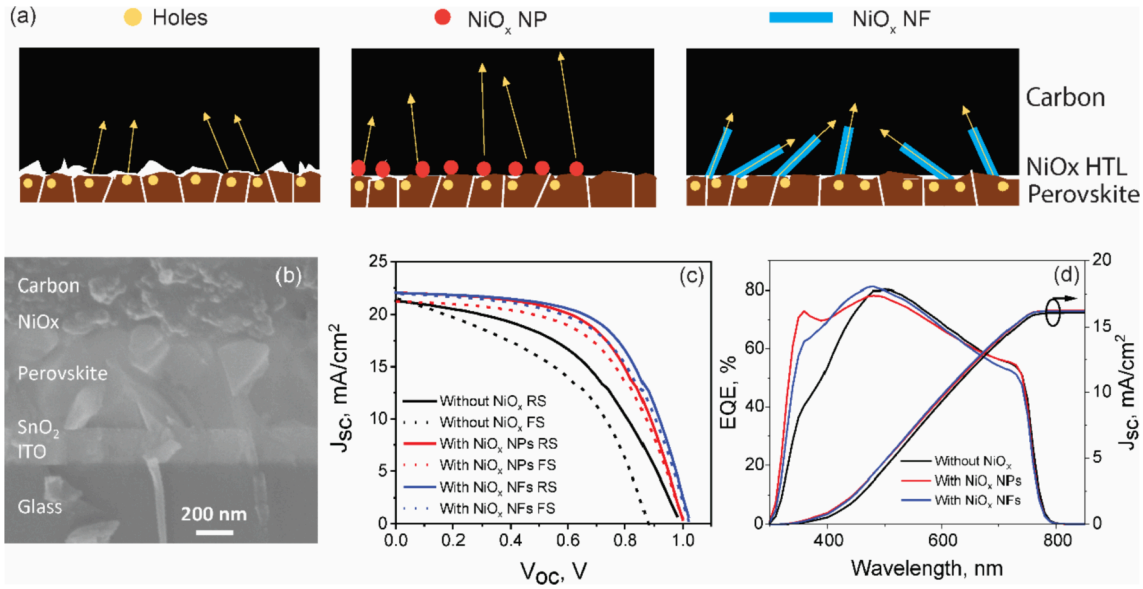

Fig. 4. (a) Schematic illustration of hole extraction with and without NiO_x HTL, (b) J-V curves with forward and reverse scan, and (c) external quantum efficiency (EQE) spectra of the champion cells with and without NiO_x layer with the integrated current.

perovskite upon absorption of the incoming solar spectrum, and the generated holes diffuse to the carbon electrode. In the case of bare perovskite, since both the perovskite and carbon surfaces are rough, the effective area of contact at this interface is limited, and hence inefficient extraction of holes occurs. When the pristine perovskite film was covered with NiO_x NPs, the surface becomes much smoother, and hence holes can be easily extracted, thereby improving the performance of the device. When NFs are deposited on the perovskite film, the surface roughness increases even further. But this turns out to be an advantage as the increased roughness is due to the fibers standing out of the plane. As shown in Fig. 4(b), the introduction of NiOx nanofibers makes the interface between the carbon and perovskite denser, and hence the effective surface area of contact between the carbon and NFs increases, thereby improving the hole extraction capability. Moreover, the diffusion of holes is highly directional since NiOx NFs are highly directional (1D), which can enable a faster extraction of holes.

To validate our hypothesis, we fabricated PSCs with NiO_x NFs/NPs as HTL with an n-i-p structure configuration of ITO/SnO_2/perovskite/NiO_x/Carbon, where a 25 μm thick carbon was doctor bladed as the counter electrode as shown in Fig. 4(b). The device performance with HTL-free PSCs is shown in Fig. 4(c) with reverse and forward scan. Firstly, we optimize the performance for NiO_x-based devices for different thicknesses of NiOx HTL by varying the spin-coating speed from 2000 to 4000 r.p.m. As shown in supporting information Table S1, devices with NPs and NFs deposited at 3000 r.p.m. recorded the best PCE due to the impressive J_{sc} and FF. The electrical parameters of the champion devices for each condition are summarized in Table 1. PSCs fabricated with NiO_x HTL demonstrated a significant increase in open-circuit voltage (V_{oc}), fill factor (FF), and PCE. The champion cell with NiO_x NFs and NPs had recorded a 26.37% and 21.87% improvement in PCE respectively when compared with the reference cell without NiOx HTLs. The significant boost in PCE can be attributed to the drastic improvement in V_{oc} and FF of the devices due to the efficient extraction of holes by NiO_x NFs/NPs, and thereby avoiding the non-radiative recombination with electrons that might have occurred had they not been extracted, as in the case of reference cells. Particularly, both NiOx HTLs can also address the hysteresis issue of the current voltage curve of the HTL-free carbon-based perovskite. Supporting information Table S2 shows the electrical parameters of the champion cells under reverse scan (RS) and forward scan (FS). Hysteresis index (HI) was calculated using equation (1) to estimate the hysteresis changes.

$$HI = \frac{PCE_{reverse} - PCE_{forward}}{PCE_{reverse}} \quad (1)$$

where $PCE_{reverse}$ and $PCE_{forward}$ are the calculated PCE by RS and FS, respectively. Larger HI values correlate with increased hysteresis. As shown in Table S2, devices without NiO_x shows the highest HI of 17.01%. The devices with NPs and NFs had much lower HI of 6.9% and 5.97% respectively. The significant hysteresis for NiO_x-free devices is associated with the poor interface between the perovskite and carbon electrode, which affects the carrier transport via the interface. The drastically improved interfacial contacts for NiO_x-based devices led to reduced hysteresis with better carrier transport.

External quantum efficiency (EQE) spectra of the champion devices are shown in Fig. 5(c), where integral photocurrents as a function of wavelength are also presented. It is shown that the perovskite devices with NiOx HTLs shown improved EQE at short wavelength (<500 nm). The integrated photocurrent densities have a relatively smaller integrated EQE current density compared with the J_{sc} derived from J-V curves due to the poor reflectivity of the carbon electrode to sunlight and the perovskite/carbon interface still need to be improved (Peng et al., 2021).

EIS measurements were used to study the carrier recombination behavior in the devices. The Nyquist plots of perovskite devices with different HTL at an applied bias voltage of 0.5 V under dark conditions are shown in supporting information Fig. S4. The obtained data were fitted using Z-View software according to a simplified equivalent circuit. The semicircles at high frequency under dark conditions correspond to the recombination resistance (R_{rec}), and the devices with NiO_x HTL show the maximum R_{rec} (Zhou et al., 2019). This increased R_{rec} signifies a better interfacial contact, reduced carrier recombination, and efficient extraction of charge carriers after the incorporation of NiO_x. These results are consistent with the device performance, which is further proof that adding the NiO_x layer can improve the electrical performance of the

Table 1
Electrical parameters of champion devices with and without NiO_x NFs and NPs.

Cells	V_{oc}, V	J_{sc}, mA/cm^2	FF, %	PCE, %
Without NiOx	0.99	21.21	48.04	10.11
With NiOx NPs	1.0	22.07	58.4	12.94
With NiOx NFs	1.03	22.07	60.62	13.73

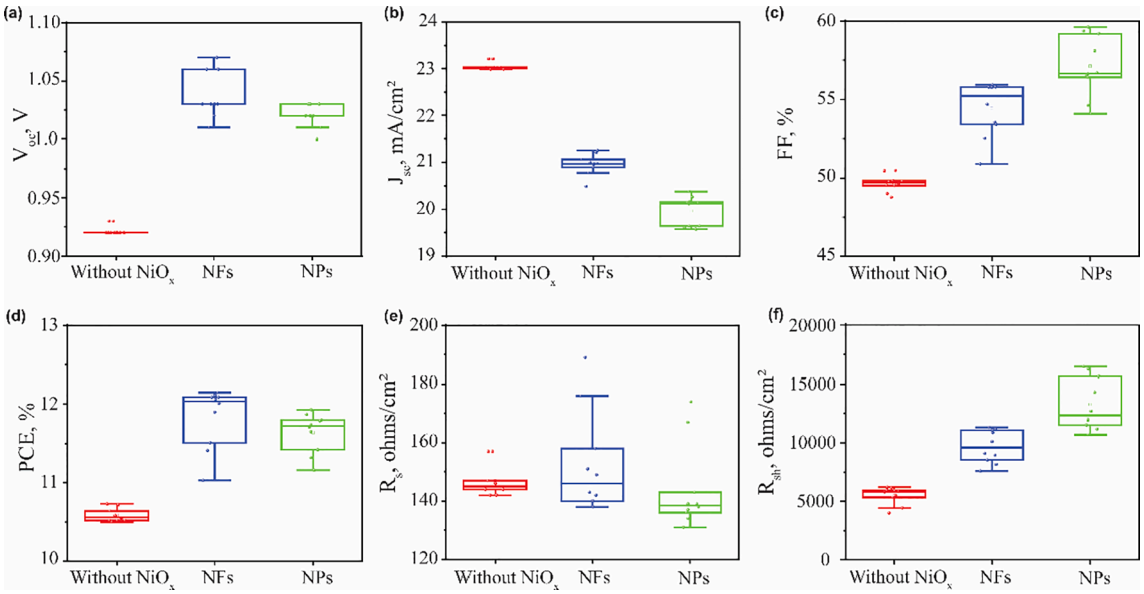

Fig. 5. Statistical distribution of (a) V_{oc}, (b) J_{sc}, (c) FF, (d) PCE, (e) R_s, and (f) R_{sh} of PSCs with and without NiO_x NFs/NPs as HTLs.

devices.

To study about the reproducibility of the devices, we fabricated 10 cells each for the three different conditions: PSC without HTL (Reference), and PSCs with NiOx NFs and NPs as HTL. It is clear from the distribution that the average PCE of the devices with NiOx NFs as HTL is higher than the average PCE for reference cells as well as cells with NP HTL. This, along with the slightly reduced R_s, and hugely increased R_{sh} (by almost 2–3 folds) is due to the improved interfacial contact with the carbon electrode which accelerates the hole extraction, and due to the inherent ability of NiO_x to block the electrons. The boost in the V_{oc} indicates that non-radiative recombination has been suppressed due to the electron blocking ability of the HTL.

Fig. 6(a) shows the energy diagram in the NiOx HTL based perovskite solar cells, where the NiOx could promote the carrier extraction with desired band alignment. In addition, it is expected that the NiOx HTL can also improve the device stability due to the improved interface to prevent moisture and oxygen attack the perovskite layer. Fig. 6(b) shows the device stability of the planar carbon-based PSCs based on NiO_x as HTL. The non-encapsulated device performance under ambient conditions (humidity: ca. 60%) without illumination for 120 h. The PCE of the device without NiO_x started dropping faster than the devices with NiO_x. However, all these devices had >90% initial PCE even after 120 h of storage. This is evidence that all the devices show excellent stability against moisture regardless of NiO_x due to the carbon electrode which acts as a good hydrophobic barrier layer inhibiting water-indicated degradation of perovskite film. The initial accelerated degradation of the device without NiO_x under light can be attributed to the unfavorable ion diffusion from perovskite films to the electrodes. NiO_x may hinder the iodide escape from perovskite film, thus suppressing the sudden degradation of device performance (Chu et al., 2019).

4. Conclusions

In summary, we introduced the NiO_x NFs as the HTLs for the planar carbon-based n-i-p PSCs. The overall efficiency of carbon-based PSC was enhanced by the inclusion of NiO_x NF/NP HTL deposited on the perovskite layer. The interfacial contact was improved between the perovskite and carbon, which enhanced the hole extraction capability of the counter electrode. This contributed to the enhancement in the electrical characteristics of the devices compared to HTL-free devices, achieving a champion efficiency of 13.73% with NiO_x NFs and 12.94% with NPs, as compared to only 10.11% without HTL. This work demonstrates that NiOx NFs is a suitable candidate for carbon-based perovskite with prolonged stability.

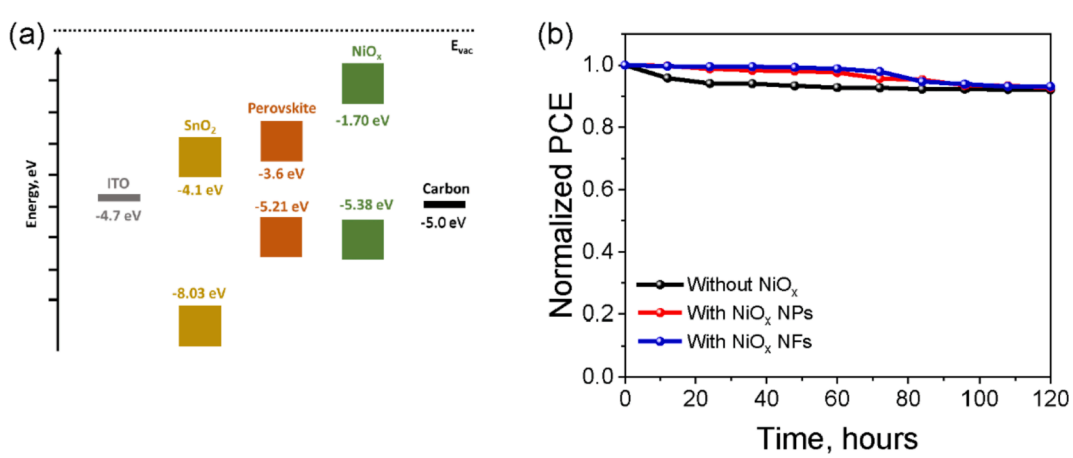

Fig. 6. (a) Energy diagram of the NiOx HTL in the perovskite solar cells, and (b) stability test of the perovskite solar cells without and with the NiOx NP and NF HTLs, respectively.

Author contribution

Prof. Feng Yan designed the research and S. N. Vijayaraghavan, Jacob Wall, Harigovind G. Menon Liping Guo, Al Amin, and Xiao Han, and Xiaomeng Duan- performed research, analyzed data, and revised the manuscript. Prof. Lingyan Kong, Yufeng Zheng and. Lin Li helped performed research and review & edit the manuscript.

Declaration of Competing Interest

The authors declare that they have no known competing financial interests or personal relationships that could have appeared to influence the work reported in this paper.

Acknowledgments

This work is supported by National Science Foundation under contract No. 1944374, 2039883, and 2019473, National Aeronautics and Space Administration, Alabama EPSCoR International Space Station Flight Opportunity program (contract# 80NSSC20M0141), and USDA National Institute of Food and Agriculture, AFRI project award (contract# 2020-67022-31376).

Appendix A. Supplementary material

Supplementary data to this article can be found online at https://doi.org/10.1016/j.solener.2021.10.039.

References

Angel, N., Vijayaraghavan, S., Yan, F., Kong, L., 2020. Electrospun cadmium selenide nanoparticles-loaded cellulose acetate fibers for solar thermal application. Nanomaterials 10 (7), 1329.
Bokuniaeva, A.O., Vorokh, A.S., 2019. Estimation of particle size using the Debye equation and the Scherrer formula for polyphasic TiO2 powder. J. Phys. Conf. Ser. 1410, 012057.
Brockner, W., Ehrhardt, C., Gjikaj, M., 2007. Thermal decomposition of nickel nitrate hexahydrate, Ni(NO3)2·6H2O, in comparison to Co(NO3)2·6H2O and Ca(NO3) 2·4H2O. Thermochim Acta 456 (1), 64–68.
Chu, Q.-Q., Ding, B., Peng, J., Shen, H., Li, X., Liu, Y., Li, C.-X., Li, C.-J., Yang, G.-J., White, T.P., Catchpole, K.R., 2019. Highly stable carbon-based perovskite solar cell with a record efficiency of over 18% via hole transport engineering. J. Mater. Sci. Technol. 35 (6), 987–993.
Guo, L., Vijayaraghavan, S.N., Duan, X., Menon, H.G., Wall, J., Kong, L., Gupta, S., Li, L., Yan, F., 2021. Stable and efficient Sb2Se3 solar cells with solution-processed NiOx hole-transport layer. Sol. Energy 218, 525–531.
Habisreutinger, S.N., Blackburn, J.L., 2021. Carbon nanotubes in high-performance perovskite photovoltaics and other emerging optoelectronic applications. J. Appl. Phys. 129 (1), 010903.
Hadadian, M., Smått, J.-H., Correa-Baena, J.-P., 2020. The role of carbon-based materials in enhancing the stability of perovskite solar cells. Energy Environ. Sci. 13 (5), 1377–1407.
Harilal, M., Krishnan, S.G., Vijayan, B.L., Reddy, M.V., Adams, S., Barron, A.R., Yusoff, M.M., Jose, R., 2017. Continuous nanobelts of nickel oxide–cobalt oxide hybrid with improved capacitive charge storage properties. Mater. Des. 122, 376–384.
Hawash, Z., Ono, L.K., Qi, Y., 2018. Recent Advances in Spiro-MeOTAD Hole Transport Material and Its Applications in Organic-Inorganic Halide Perovskite Solar Cells. Adv. Mater. Interfaces 5 (1), 1700623.
Hayat, A., Mane, S.K.B., Shaishta, N., Khan, J., Hayat, A., Keyum, G., Uddin, I., Raziq, F., Khan, M., Manjunatha, G., 2019. Nickel oxide nano-particles on 3D nickel foam substrate as a non-enzymatic glucose sensor. J. Electrochem. Soc. 166 (15), B1602.
Hosny, N.M., 2011. Synthesis, characterization and optical band gap of NiO nanoparticles derived from anthranilic acid precursors via a thermal decomposition route. Polyhedron 30 (3), 470–476.
Icli, K.C., Ozenbas, M., 2018. Fully metal oxide charge selective layers for nip perovskite solar cells employing nickel oxide nanoparticles. Electrochim. Acta 263, 338–345.
Langford, J.I., Wilson, A.J.C., 1978. Sherrer formula after 60 years. J. Appl. Crystal. 11, 102–113.
Jeng, J.Y., Chen, K.C., Chiang, T.Y., Lin, P.Y., Tsai, T.D., Chang, Y.C., Guo, T.F., Chen, P., Wen, T.C., Hsu, Y.J., 2014. Nickel oxide electrode interlayer in CH3NH3PbI3 perovskite/PCBM planar-heterojunction hybrid solar cells. Adv. Mater. 26 (24), 4107–4113.
Jung, H.S., Park, N.G., 2015. Solar Cells: Perovskite Solar Cells: From Materials to Devices (Small 1/2015). Small 11 (1), 2–2.
Kaneko, R., Kanda, H., Sugawa, K., Otsuki, J., Islam, A., Nazeeruddin, M.K., 2019. Perovskite solar cells using surface-modified NiOx nanoparticles as hole transport materials in n-i-p configuration. Solar RRL 3 (9), 1900172.
Khalil, A., Hashaikeh, R., Jouiad, M., 2014. Synthesis and morphology analysis of electrospun copper nanowires. J. Mater. Sci. 49 (8), 3052–3065.
Kim, Y.S., Yu, B.-K., Kim, D.-Y., Kim, W.B., 2011. A hybridized electron-selective layer using Sb-doped SnO2 nanowires for efficient inverted polymer solar cells. Sol. Energy Mater. Sol. Cells 95 (10), 2874–2879.
Liu, H., Wang, X., He, G., Lin, Y., Wei, J., Zheng, J., Zheng, G., Sun, D., Electrospun nickel oxide nanofibers for gas sensor application. In: The 8th Annual IEEE International Conference on Nano/Micro Engineered and Molecular Systems.
Liu, Y., Li, J., Zhou, B., Chen, H., Wang, Z., Cai, W., 2011. A TiO 2-nanotube-array-based photocatalytic fuel cell using refractory organic compounds as substrates for electricity generation. Chem. Commun. 47 (37), 10314–10316.
Macdonald, T.J., Xu, J., Elmas, S., Mange, Y.J., Skinner, W.M., Xu, H., Nann, T., 2014. NiO Nanofibers as a Candidate for a Nanophotocathode. Nanomaterials 4 (2), 256–266.
Manders, J.R., Tsang, S.W., Hartel, M.J., Lai, T.H., Chen, S., Amb, C.M., Reynolds, J.R., So, F., 2013. Solution-processed nickel oxide hole transport layers in high efficiency polymer photovoltaic cells. Adv. Funct. Mater. 23 (23), 2993–3001.
Nakasa, A., Suzuki, E., Usami, H., Fujimatsu, H., 2005. Synthesis of porous nickel oxide nanofiber. Chem. Lett. 34 (3), 428–429.
Peck, M.A., Langell, M.A., 2012. Comparison of nanoscaled and bulk NiO structural and environmental characteristics by XRD, XAFS, and XPS. Chem. Mater. 24 (23), 4483–4490.
Peng, C., Su, H., Li, J., Duan, Q., Li, Q., Xiao, J., Ku, Z., Zhong, J., Li, W., Peng, Y., 2021. Scalable, efficient and flexible perovskite solar cells with carbon film based electrode. Sol. Energy Mater. Sol. Cells 230, 111226.
Saranin, D., Komaricheva, T., Luchnikov, L., Muratov, D.S., Le, T.S., Karpov, Y., Gostishchev, P., Yurchuk, S., Kuznetsov, D., Didenko, S., 2021. Hysteresis-free perovskite solar cells with compact and nanoparticle NiO for indoor application. Sol. Energy Mater. Sol. Cells 227, 111095.
Schulz, P., Dowgiallo, A.-M., Yang, M., Zhu, K., Blackburn, J.L., Berry, J.J., 2016. Charge Transfer Dynamics between Carbon Nanotubes and Hybrid Organic Metal Halide Perovskite Films. J. Phys. Chem. Lett. 7 (3), 418–425.
Shim, H.-S., Kim, J.W., Sung, Y.-E., Kim, W.B., 2009. Electrochromic properties of tungsten oxide nanowires fabricated by electrospinning method. Sol. Energy Mater. Sol. Cells 93 (12), 2062–2068.
Sigmund, W., Yuh, J., Park, H., Maneeratana, V., Pyrgiotakis, G., Daga, A., Taylor, J., Nino, J.C., 2006. Processing and structure relationships in electrospinning of ceramic fiber systems. J. Am. Ceram. Soc. 89 (2), 395–407.
Singh, M., Yang, R.-T., Weng, D.-W., Hu, H., Singh, A., Mohapatra, A., Chen, Y.-T., Lu, Y.-J., Guo, T.-F., Li, G., 2021. Low-temperature processed bipolar metal oxide charge transporting layers for highly efficient perovskite solar cells. Sol. Energy Mater. Sol. Cells 221, 110870.
Vijayaraghavan, S., Wall, J., Li, L., Xing, G., Zhang, Q., Yan, F., 2020. Low-temperature processed highly efficient hole transport layer free carbon-based planar perovskite solar cells with SnO2 quantum dot electron transport layer. Materials Today Physics 13, 100204.
Wang, S., Huang, Z., Wang, X., Li, Y., Günther, M., Valenzuela, S., Parikh, P., Cabreros, A., Xiong, W., Meng, Y.S., 2018. Unveiling the role of tBP–LiTFSI complexes in perovskite solar cells. J. Am. Chem. Soc. 140 (48), 16720–16730.
Wang, Y., Santiago-Avilés, J.J., 2003. Synthesis of lead zirconate titanate nanofibres and the Fourier-transform infrared characterization of their metallo-organic decomposition process. Nanotechnology 15 (1), 32–36.
Wang, Y., Wu, J., Zhang, P., Liu, D., Zhang, T., Ji, L., Gu, X., David Chen, Z., Li, S., 2017. Stitching triple cation perovskite by a mixed anti-solvent process for high performance perovskite solar cells. Nano Energy 39, 616–625.
Xia, Y., Yang, P., Sun, Y., Wu, Y., Mayers, B., Gates, B., Yin, Y., Kim, F., Yan, H., 2003. One-dimensional nanostructures: synthesis, characterization, and applications. Adv. Mater. 15 (5), 353–389.
Yoo, J.J., Seo, G., Chua, M.R., Park, T.G., Lu, Y., Rotermund, F., Kim, Y.-K., Moon, C.S., Jeon, N.J., Correa-Baena, J.-P., Bulović, V., Shin, S.S., Bawendi, M.G., Seo, J., 2021. Efficient perovskite solar cells via improved carrier management. Nature 590 (7847), 587–593.
Zang, L., Zhu, J., Xia, Y., 2014. Facile synthesis of porous NiO nanofibers for high-performance supercapacitors. J. Mater. Eng. Perform. 23 (2), 679–683.
Zhang, L., Hu, J., Voevodin, A.A., Fong, H., 2010. Synthesis of continuous TiC nanofibers and/or nanoribbons through electrospinning followed by carbothermal reduction. Nanoscale 2 (9), 1670–1673.
Zhou, J., Wu, J., Li, N., Li, X., Zheng, Y.-Z., Tao, X., 2019. Efficient all-air processed mixed cation carbon-based perovskite solar cells with ultra-high stability. J. Mater. Chem. A 7 (29), 17594–17603.